A new approach for GNSS tomography from a few GNSS stations

Nan Ding[1, 2], Shubi Zhang[1], Suqin Wu[2], Xiaoming Wang[3], Xin Liu[1], Allison Kealy[4], Kefei Zhang[2]

[1] School of Environment Science and Spatial Informatics, China University of Mining and Technology, Xuzhou, China

[2] SPACE Research Centre, School of Mathematical and Geospatial Sciences, RMIT University, Melbourne, Victoria, Australia

[3] Academy of Opto-Electronics, Chinese Academy of Sciences, Beijing 100094, China

[4] Geospatial Science, School of Science, RMIT University, Melbourne, Victoria, Australia

Correspondence: Kefei Zhang (kefei.zhang@rmit.edu.au); Nan Ding (metdingnan@163.com)

Abstract

The determination of the distribution of water vapor in the atmosphere plays an important role in the atmospheric monitoring. Global Navigation Satellite Systems (GNSS) tomography can be used to construct 3D distribution of water vapor over the field covered by a GNSS network with high temporal and spatial resolutions. In current tomographic approaches, a pre-set fixed rectangular field that roughly covers the area of the distribution of the GNSS signals on the top plane of the tomographic field is commonly used for all tomographic epochs. Due to too many unknown parameters needing to be estimated, the accuracy of the tomographic solution degrades. Another issue of these approaches is their unsuitability for GNSS networks with a few stations as the shape of the field covered by the GNSS signals is in fact roughly an upside-down cone rather than the rectangular cube as the pre-set. In this study, a new approach for determination of tomographic fields fitting the real distribution of GNSS signals on different tomographic planes at different tomographic epochs and also for discretization of the tomographic fields based on the perimeter of the tomographic boundary on the plane and meshing techniques is proposed. The new approach was tested using three stations from the Hong Kong GNSS network and validated by comparing the tomographic results against radiosonde data from King's Park Meteorological Station (HKKP) during the one month period of May, 2015. Results indicated that the new approach is feasible for a three-station GNSS network tomography. This is significant due to the fact that the conventional approaches cannot even solve a few stations network tomography.

1 Introduction

Information of the distribution and variation of atmospheric water vapor is essential for meteorological applications. Nowadays, the most commonly used technology for measuring atmospheric water vapor is radiosonde due to its high vertical resolution and high accuracy, even though its horizontal resolution is very low−several hundreds of kilometers, and its temporal resolution is also low−twice daily. With the development of Global Navigation Satellite Systems

40 (GNSS), using GNSS measurements to remotely sense water vapor in the atmosphere has
41 attracted significant attention due to their 24-hour availability, global coverage and low cost.
42 based on GNSS measurements collected from a regional or global GNSS reference network, a
43 regional or a global tomographic model, which is three-dimensional (3D), can be constructed.
44 The tomographic model reflects the spatial variation of water vapor in the time period
45 investigated, thus it has the potential to be used to investigate the evolution of heavy rain events
46 for severe weather forcast (Wang et al., 2017; Chen et al., 2017; Zhang et al., 2015).

47 　　　　Using the slant wet delays (SWDs) estimated from the GNSS signals of a GNSS network
48 to construct a tomographic model is called GNSS tomography. Flores et al. (2000) built the first
49 GNSS tomographic model using $4 \times 4 \times 40$ voxels and developed Local Tropospheric Tomography
50 Software (LOTTOS) for simulation and processing of GNSS data. Gradinarsky (2002) developed
51 the wet refractivity Kalman filter (WeRKaF) for tomographic inversion of GNSS data and the
52 filter mainly focused on the initialization of the tomographic covariance matrix used in the
53 implementation of the Kalman filter. Troller et al. (2006) developed the atmospheric water vapor
54 tomography software (AWATOS) based on double-differenced GPS observations and double-
55 differenced phase residuals. Rohm and Bosy (2009) addressed the issue with the ill-condition of
56 tomographic equations using the Moore-Penrose pseudo inverse of the variance-covariance
57 matrix. In order to minimize the discretization effects, Perler et al. (2011) for the first time
58 proposed using node parameterization in GNSS tomographic modeling. Chen and Liu (2014)
59 optimized a water vapor tomographic region through moving voxel location along the latitudinal
60 and longitudinal directions until the number of the voxels that contain GNSS signals reached the
61 maximum. Yao et al. (2016) improved the utilization rate of GNSS observations in the modeling
62 by adding extra voxels on the top of the tomographic region where some satellite signals partly
63 cross the tomographic field. Ding et al. (2017) developed an access order scheme called prime
64 number decomposition (PND) for minimizing the correlation between the SWDs which are the
65 sample data of tomographic modeling. The above GNSS tomographic approaches were tested
66 using various numbers of GNSS stations, majority of which were a few tens of stations, and the
67 maximum and minimum were 270 and 8 respectively.

68 　　　　In all the above tomographic approaches, the tomographic fields are all assumed
69 rectangular cubes. The size and location of the rectangular cubes are determined based on the
70 distribution of GNSS signals only on the top boundary of the tomographic field−the rectangular
71 cube that best fits the top boundary is adopted (Bastin et al., 2005; Bender et al., 2009;
72 Champollion et al., 2005; Ding et al., 2017; Gradinarsky and Jarlemark, 2004; Hoyle, 2005;
73 Rohm et al., 2014; Seko et al., 2000; Troller et al., 2006; Xia et al., 2013; Ye et al., 2016). In fact,
74 the field that GNSS signals cover has a shape of upside-down cone, roughly, meaning that in the
75 part near the edge of the cube, especially in the lower part, none of the GNSS signals cross
76 through. This region is named empty spatial region (ESR) in this paper merely for convenience.
77 In fact, the inclusion of those voxels/nodes in the ESR in the discretization of the model not only
78 does little contribution to the improvement on the accuracy of the model solution but also adds
79 extra meaningless unknown parameters to be estimated. More parameters mean more horizontal
80 constraints are needed and also degradation of the accuracy and stability of the solution,
81 especially in the case the network consists of a few stations, e.g. only three stations. This is
82 because the difference in the sizes covered by the GNSS signals in the bottom and top planes of
83 the tomographic field is large, meaning a large number of voxels/nodes in the ESR and far away
84 from the observed signals, especially in the lower part of the tomographic field. In the estimation
85 process of the model, the horizontal constraints imposed on these nodes/voxels are usually from

86 extrapolated results based on their nearest observations. If these voxels/nodes are far away from
87 the observed signals, the constraints are too weak and will cause difficulty in the solving of the
88 tomographic equations. The large number of nodes/voxels contained in ESRs stemming from a
89 small number of GNSS stations is the main reason for the unsuitable of the current GNSS
90 tomographic approaches to   using a-few-station networks.

91   In this study, a new node parameterization approach for dynamic determination of
92 tomographic fields and the discretization of the fields at each tomographic epoch was proposed.
93 It is adaptive node parameterization for varying density on different tomographic planes. This
94 differs from all current approaches in which the same pre-set rectangular cube roughly
95 determined by the distribution of the signals only on the top tomographic plane is adopted for all
96 planes and all epochs of the tomography. In addition, for the discretization of the tomographic
97 field determined for each plane at each epoch, the location and number of all the nodes on the
98 plane are determined according to the size of the tomographic field. As a result, the tomographic
99 model is tailor-made for all planes and alll epochs. Moreover, the new approach is applicable to
100 GNSS networks with any number of stations, i.e. equal to or larger than three.

101 **2 Methodology**

102 2.1 Observations of GNSS Tomography

103   GNSS signals are bent and delayed when they propagate through the atmosphere. The
104 atmosphere can be divided into the ionosphere and troposphere. The first order ionospheric delay
105 was eliminated using the so-called ionosphere-free linear combination of dual-frequency
106 observations. The tropospheric delay can be divided into two components−the dry delay and the
107 wet delay. The wet component is the SWD and can be expressed by

108 $$SWD = m_w(e) \cdot \left\{ ZWD + \left[G_N^w \cdot \cos(\phi) + G_E^w \cdot \sin(\phi) \right] \cdot \cot(e) \right\} + R \qquad (1)$$

109 where $m_w(e)$ is a wet mapping function and the VMF1 mapping function was used in this study;
110 G_N^w and G_E^w are the wet delay gradients in the north–south and east–west directions, respectively;
111 R is the post-fit residuals and in one satellite-receiver, the residuals exceeding 2.5 times the
112 standard deviation were removed and then computed means were subtracted from the remaining
113 residuals to clean observation from systematic effects; ZWD is the zenith wet delay of the GNSS
114 station, which can be obtained by subtracting the zenith hydrostatic delay (ZHD) from the zenith
115 total delay (ZTD). The ZHD can be calculated by a standard tropospheric model such as the most
116 commonly used Saastamoinen model (Saastamoinen, 1972) and the ZTD is estimated (as an
117 unknown parameter) in GNSS data processing;

118   In GNSS tomographic modeling, the SWDs of GNSS signals in a tomographic field are
119 used as the observations for the estimation of water vapor parameters in the field.

120 2.2 Tomographic modeling

121 2.2.1 General approaches

122   Voxel and node parameterization are the two common GNSS tomographic approaches. In
123 the former, the tomographic field, which is usually assumed as a rectangular cube, is divided into
124 many voxels (small rectangular cubes) and in the latter, and the field is discretized by nodes, as

125 all the black and circle nodes shown in Fig. 1. In this study, the node parameterization approach
126 was adopted due to its better fitting of the spatial correlation of water vapor.

127   In the current node parameterization approaches, if the GNSS network is very small, e.g.
128 a three-station network from the Hong Kong Satellite Positioning Reference Station Network
129 (SatRef) as shown in Fig. 1, a large number of nodes are in the ESR (see the hollow circles)
130 within the rectangular cube which is the tomographic field. These nodes, as part of the unknown
131 parameters, need to be estimated. The inclusion of these unknown parameters in the estimation
132 process does not only add more 'redundant' parameters but also degrades the accuracy of the
133 solution.
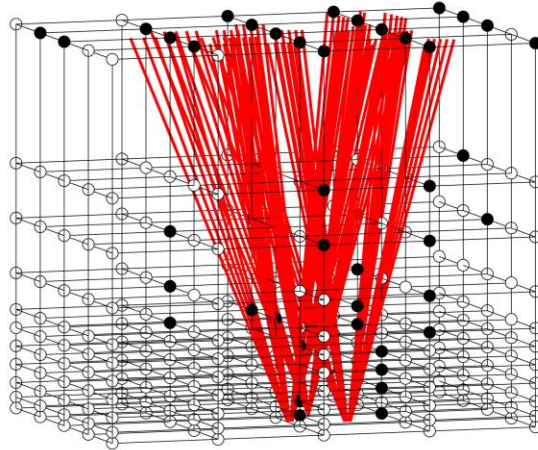
134

135 **Figure 1.** A three-station GNSS network from the Hong Kong Satellite Positioning Reference
136 Station Network (SatRef) as an example for GNSS tomography−the rectangular cube is the
137 tomographic field adopted in current node parameterization approaches, the solid nodes are those
138 near GNSS signals and the hollow nodes are those in the ESR.

139   In addition, a fixed rectangular cube is used as the tomographic field for all time in the
140 current approaches, In fact, the spatial region that the signals travel through varies with time, as
141 shown in Fig. 2 for the different distributions of the signals at the three stations shown in Fig. 1
142 on the top plane of the tomographic field at UTC 0 on 1 (day of year (DOY) 121), 16 (DOY 136)
143 and 31 (DOY 151) in May 2015.
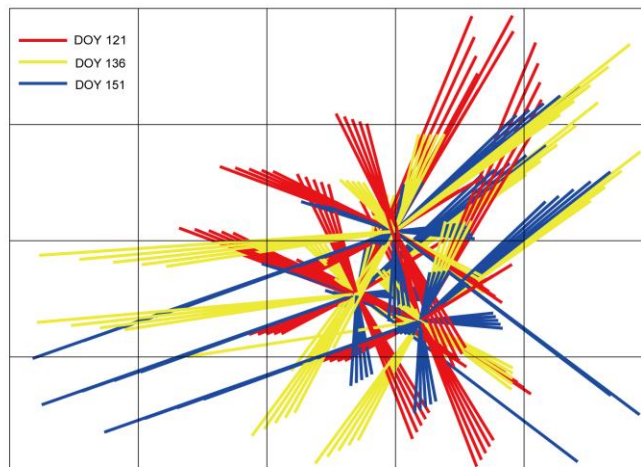
144

145 **Figure 2.** Distributions of GNSS signals at the three stations shown in Fig. 1 on the top plane of
146 the tomographic field with the sampling rate of 30 seconds at UTC 0 on 1, 16 and 31 May, 2015.

147   To address the above issues, a new node parameterization approach that dynamically
148 adjusts the tomographic field based on the spatial distribution of the GNSS signals at the
149 tomographic epoch and also dynamically adjusts the location and number of all the nodes based
150 on the size of the tomographic field is proposed. Its procedure is elaborated in the next section.

151

152 2.2.2 New approach

153   The procedure for the new approach mainly includes two steps–determination of
154 tomographic field and determination of node position, which are introduced below.

155 *i) Determination of tomographic field*

156   A tomographic field is regarded to be comprised of many layers in the vertical dimension
157 and these layers with the same or different thickness, depending on the distribution of water
158 vapor at the height of the layer, as shown in Fig. 3(a), each layer is formed by two neighboring
159 horizontal planes. After all these planes are determined, the next task is to determine the
160 tomographic boundary for each plane, according to the distribution of the GNSS signals on the
161 plane. Fig. 3(b) shows the tomographic boundary on each of the planes shown in Fig. 3(a), which
162 is determined from the following three steps that were used in the Graham scan (Graham, 1972)
163 determining all the intersections (the blue points) of the GNSS signal paths on the plane (they
164 are name pierce points in this paper); 2) using a stack of the pierce points to detect and remove
165 all those pierce points that are in concavities; and 3) connecting the rest pierce points to form a
166 convex hull, which is the tomographic boundary (black polygon).
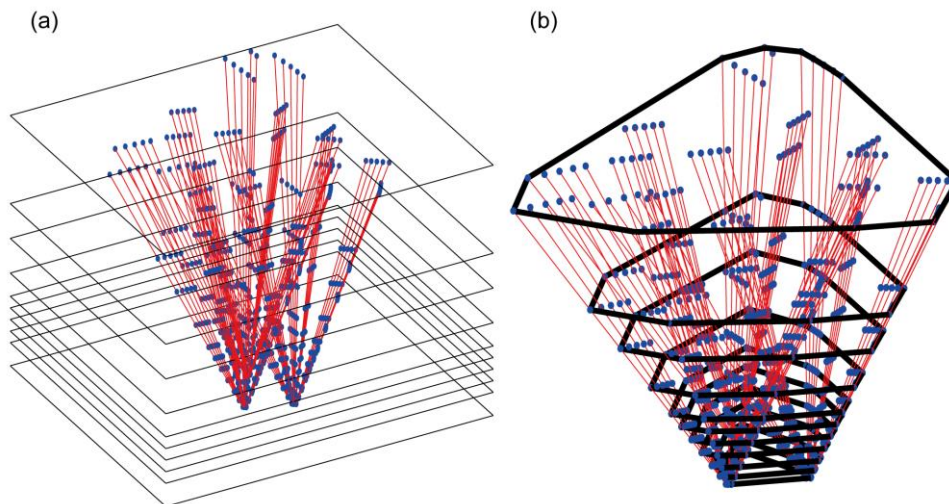
168 **Figure 3.** (a) A tomographic field is divided by many layers, the thickness of which is dependent
169 upon the distribution of water vapor in the layer, the red lines are the sampling GNSS signals and
170 the blue points are the intersections of the GNSS signals on each horizontal plane; and (b)
171 Tomographic boundary is depicted by the black polygon on each horizontal plane.

172

173   Since the shape of the tomographic boundary determined using the new approach is irregular,
174   it is difficult to generate equidistant nodes within the boundary. This differs from current node
175   parameterization approaches in which uniformly distributed nodes can be easily pre-set. In this
176   study meshing techniques are used to adjust the position of nodes for each plane and each
177   tomographic epoch, and their procedure is discussed in the next section.

178   *ii) Determination of node position*

179   Meshing techniques for the generation of equidistant nodes of a GNSS tomographic
180   model include three steps and each of the steps is introduced below.
181   1) A mesh background in a desired size with nodes is used to provide initial nodes for
182   each plane see Fig. 4(a) where the polygon is obtained from the last section for the tomographic
183   boundary on the plane and at all the vertices of the polygon a new set of nodes are also attached
184   to the initial nodes, see Fig. 4(b) for the final initial nodes.

185   2) Delaunay triangulation (Delaunay, 1934) is used to establish a topology for the above
186   initial nodes on each plane. It determines non-overlapping triangles that fill the region in a
187   polygon such that every edge is shared by at most two triangles and none of the vertices is inside
188   the circumcircle of any of the triangles. Delaunay triangulations maximize the minimum angle of
189   all the triangles to avoid sliver triangles which has undesirable properties during some
190   interpolation or rasterization processes (Edelsbrunner et al., 2000). Several methods have been
191   developed to compute the Delaunay triangulation such as the commonly used flipping edges and
192   conversing a Voronoi diagram. In this study, the flipping edges method is adopted to connect the
193   initial nodes shown in Fig. 4(b) by the edges of Delaunay triangles on each plane and the
194   topology formed is shown in Fig. 4(c).

195   3) The force displacement algorithm (Persson, 2005) is applied to the above topology for
196   the adjustment of the initial nodes into equidistance with a reasonable length fitting the size of
197   the tomographic boundary on each plane. This method is based on the assumption that each edge
198   in the topology has a force value (let it be F_{ij}) equal to the length of the edge. It can be used to
199   make all the edges' F_{ij} close to the same and reasonable pre-set force value F_0 for a (roughly)
200   regularly distributed mesh. This is the main reason for the introducing of this method to this
201   study for adjusting the nodes in the irregular tomographic boundary (like Fig. 4(c)) into
202   equidistance (roughly). The force displacement algorithm is an iterative process as:

203
$$[X^k \quad Y^k] = [X^{k-1} \quad Y^{k-1}] + Scal \cdot [F_x^{\;k} \quad F_y^{\;k}] \tag{2}$$

204   where X^k and Y^k are the vectors of the x and y coordinates respectively of all the nodes on the
205   plane at the kth iteration and k-1 denotes the previous iteration; *Scal* is a relaxation factor for
206   constraining the amount of the movement from the k-1th iteration to an appropriate value, for
207   which a 0.2 value is commonly used; $F_x^{\;k}$ is the vector of the vector sums of all the forces
208   working on each of the nodes in the x direction, $F_y^{\;k}$ is that in the y direction.

209   After the above algorithm is performed, all the nodes on the plane can be adjusted from
210   the initial position (Fig. 4(c)) to equidistant position (Fig. 4(d)) through a series of iterations.

211   It is noted that the sizes of the tomographic boundaries on different planes are different
212   (Fig. 3(b)) while the numbers of the signals on different planes are the same, so the densities of
213   the signals on different planes are different, and the densities of the nodes on different planes

6

214 better be different through using different F_0 values. In this study, the F_0 value for the *i*th plane is
215 calculated by:

$$F_0^i = C \cdot \text{mean}(Ls^i) \tag{3}$$

217 where C is a constant coefficient and 0.68 is adopted for all planes; and $\text{mean}(Ls^i)$ is the mean of
218 all the lengths of the edges on the polygon.
219
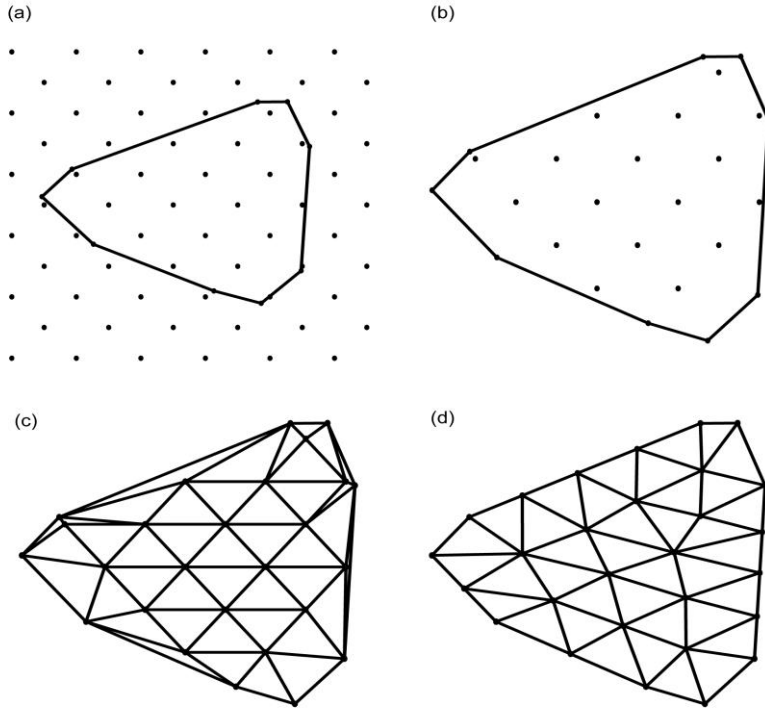
221 **Figure 4.** (a) Two sets of nodes for initialization−one set is generated using a mesh background
222 with a desired size which is usually slightly larger than the region of the GNSS signals at all time
223 and the other set is at all the vertices of the polygon (all black points); (b) Initial nodes; (c)
224 Topology formed using Delaunay triangulation; (d) Nodes with equidistance adjusted based on
225 the force displacement algorithm.

226 2.3 Observation equations

227 After equidistant nodes for all planes are determined (like Fig. 4(d)), the next step is to
228 estimate water vapor parameters at these nodes from observation equations of GNSS-derived
229 *SWDs*. The derivation of the observation equations is as follows.

230 Theoretically, *SWD* is defined as the integral of wet refractivity N_w along the signal path s

$$SWD = 10^{-6} \cdot \int_s N_w ds \tag{4}$$

232 It can be further decomposed into integrations of *n* layers:

$$233 \qquad SWD = \sum_{i=1}^{n} \int_{s_i}^{s_{i+1}} N_w^s(i)ds = \sum_{i=1}^{n} SWD_i \qquad (5)$$

234   where $N_w^s(i)$ is wet refractivity in the ith layer ; s_i, s_{i+1} are the start and end points of the
235   layer/integral; and SWD_i is the part of the SWD in the ith layer

236   In GNSS tomography, in each of the piecewise integrals expressed in Eq. (5), i.e. SWD_i,
237   the signal path in the layer is further divided into several equally spaced points and then SWD_i is
238   approximated as a function of wet refractivity at these points using the Newton-Cotes formulae
239   (Perler et al., 2011). In this study, SWD_i is approximated by the Newton-Cotes formulae of 4
240   degree at five equally spaced points, as (P_1..., P_5) shown in Fig. 5 where the plane i and plane
241   (i+1) are the two horizontal planes corresponding to the above s_i, s_{i+1} respectively, and the black
242   solid dots denote some of the equidistant nodes obtained from Fig. 4(d).

243   The methods for obtaining wet refractivity at each of the points are as follows.

244   i) Wet refractivity at points P_1 and P_5 (which are on the ith and $(i + 1)$th planes
245   respectively) can be calculated using the interpolation method of the inverse-distance-weighted
246   (IDW) mean of the sample wet refractivity data from its surrounding nodes:
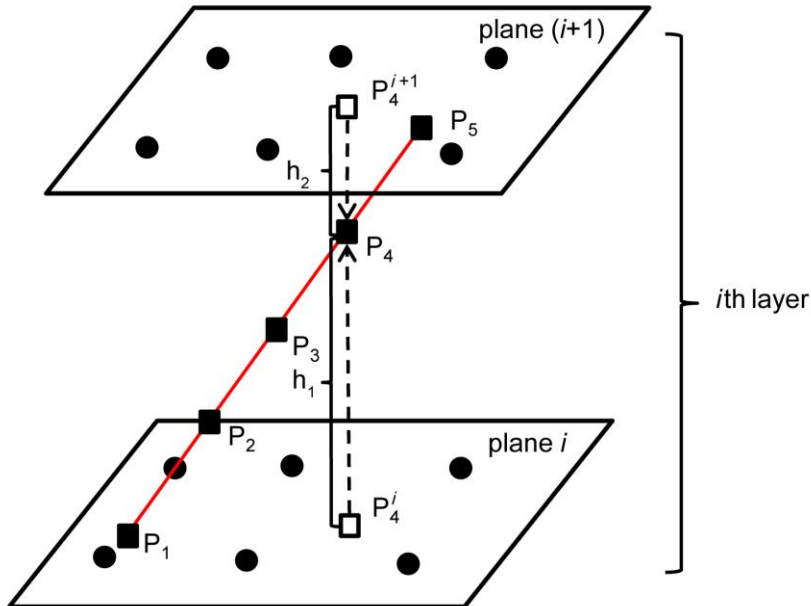
$$247 \qquad P_{wet} = \frac{\sum_{j=1}^{m} w_j \cdot n_j^{wet}}{\sum_{j=1}^{m} w_j} \qquad (6)$$

248   where j is the index of the sample data, and w_j is its weight determined by the inverse-distance;
249   and m is the number of the sample data.

250

Figure 5. Five equally spaced points (black solid squares) for an approximation of wet
refractivity for the ith layer. P_4^i and P_4^{i+1} (black hollow squares) are the projected points of P_4 on
the ith and $(i$+1)th planes respectively, h_1 is the height difference between P_4 and P_4^i , and h_2 is
that between P_4 and P_4^{i+1} .

255   ii) Wet refractivity at points P_2, P_3 and P_4, cannot be directly interpolated like that for P_1
256   and P_5, the following three-step procedure needs to be performed (P_4 is taken as an example): 1)
257   the position of P_4 is projected onto both the ith and $(i+1)$th planes to obtain two projected points
258   named P_4^i and P_4^{i+1}, respectively; 2) the above interpolation procedure for P_1 and P_5 is used to
259   obtain wet refractivity P_{4wet}^i and P_{4wet}^{i+1} at P_4^i and P_4^{i+1} respectively; and 3) P_{4wet}^i and P_{4wet}^{i+1} are used to
260   obtain a weighed mean wet refractivity for the position of P_4 using [Reitan, 1963; Tomasi, 1981]:

261
$$P_4 = \frac{|h_1|}{(|h_1|+|h_2|)} P_{4wet}^i \cdot e^{-h_1/H} + \frac{|h_2|}{(|h_1|+|h_2|)} P_{4wet}^{i+1} \cdot e^{-h_2/H} \tag{7}$$

262   where h_1 is the height difference between P_4 and P_4^i and h_2 is that between P_4 and P_4^{i+1}; and H is
263   water vapor scale height, which can be calculated by Tomasi [1977]:

264
$$H = \frac{10W}{\rho_s} \tag{8}$$

265   where W and ρ_s are the vertical total water vapor content (in g m^{-2}) and surface humidity (in g m^{-3})
266   respectively, and both can be obtained from GNSS data.

267

268   After the above procedures are carried out, SWD_i can be expressed as a function of wet
269   refractivity at a set of nodes. This procedure needs to be performed for all SWD_i ($i=1,2,..n$), then
270   the next step is to substitute these SWD_i expressions and the SWD observation into Eq. (5), to
271   form its GNSS tomographic observation equation.

272   The final GNSS tomographic observation equations of all SWDs from the GNSS network
273   for the tomographic modeling is expressed as:

274
$$A \cdot X = b \tag{9}$$

275   where A is the coefficient matrix of the model; b is the vector of the SWD observations; and X is
276   the vector of the wet refractivity parameters at all nodes.

277   The X vector in Eq. (9) can be estimated using the least squares method. However, due to
278   the problem with the sparseness of A, the algebraic reconstruction technique (ART) was used to
279   estimate X in this study.

280   2.4 Tomographic solution

281   The ART has been successfully applied to reconstruction of water vapor field (Chen and
282   Liu, 2014; Bender et al., 2011). Its main advantage is the high numerical stability, even under
283   adverse conditions and also relatively easy to incorporate prior knowledge into the reconstruction
284   process. The ART used to solve Eq. (9) is (Kaczmarz, 1937):

285
$$x^{k+1} = x^k + \lambda \frac{b_i - \langle a_i, x^k \rangle}{\|a_i\|_2^2} a_i \qquad i = 1, 2, \cdots, m \tag{10}$$

286   where a_i and b_i denote the ith rows in A and b respectively; x_k is the kth iterative solution; and λ is
287   a relaxation factor and the value of 0.2 was selected in this study.

288   It is noted that Eq. (9) needs to be sorted in a certain sequence for Eq. (10). This is
289 different from the commonly used observation equation system in which the order of the
290 observation equations is not a matter. In this study, an access order scheme based on prime
291 number decomposition (PND) proposed in (Ding et al., 2017) was used for the ordering of the
292 observation equations such that the observation equations between two consecutive iterations are
293 largely uncorrelated.

294   The unknown parameters X solved from Eq. (10) are the wet refractivity values at all
295 tomographic nodes. In some meteorological applications, water vapor density may be preferred,
296 in this case X needs to be converted using a conversion factor Π which is a function of water-
297 vapor-weighted-mean temperature Tm (Bevis et al., 1994; Wang et al., 2016) at the position of
298 the nodes.

299 **3 Test results**

300 3.1 Data selection and tomographic scheme

301   Test data used in this study were from three stations in the Hong Kong Satellite
302 Positioning Reference Station Network (SatRef), and the horizontal and vertical distributions of
303 the three stations are presented in Fig. 6(a) and Fig. 6(b), respectively. The area of our interest
304 ranges from 113.749 °E to 114.474 °E in the longitudinal direction, from 22.115 °N to 22.651 °N
305 in the latitudinal direction and from 0 to 10800 m in the vertical direction. Radiosonde data from
306 King's Park Meteorological Station (HKKP) (the blue triangle shown in Fig. 6(a) were used as
307 the reference for the validation of our test results.

308
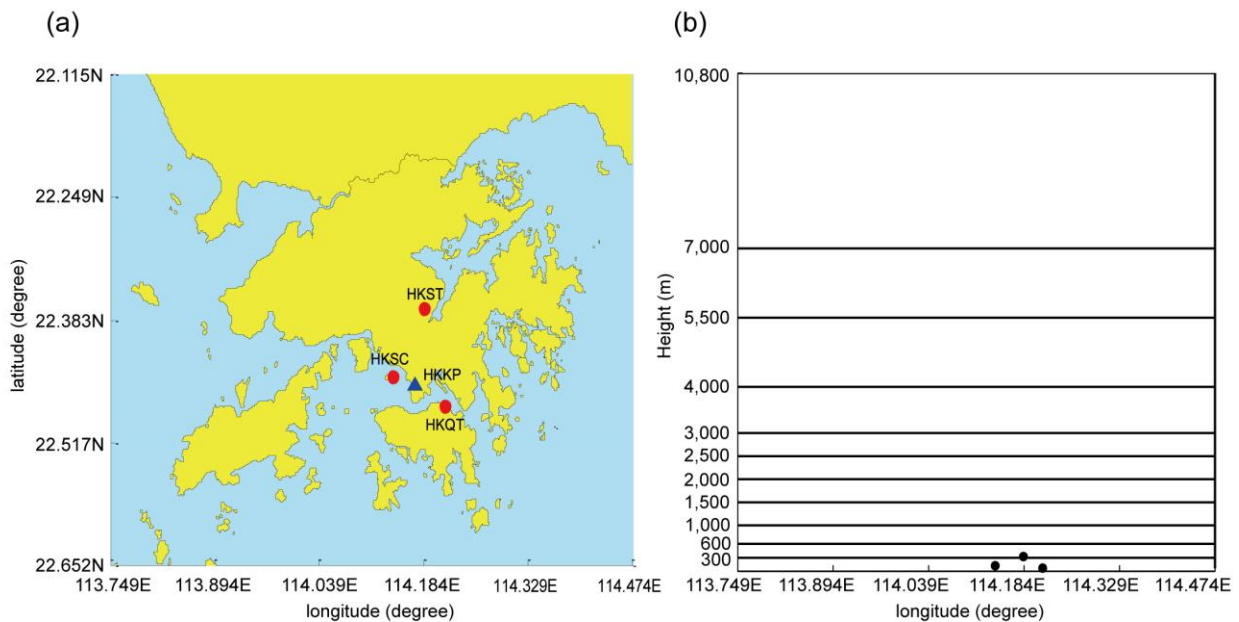
309 **Figure 6.** (a) Horizontal distribution of the three stations selected from the Hong Kong reference
310 stations (red dots) and HKKP (blue triangle); and (b) Vertical distribution of the three stations
311 (black spots) and vertical layers used in tomographic modeling.

312   The test data were from the whole month of May, 2015 (day of year (DOY) 121−151)
313 with the sampling rate of 30 seconds, and the GAMIT software was used to obtain SWDs at the

10

314 same rate in the data processing. For the tomographic modeling, a 5-minute sampling rate for
315 SWDs and a 30-minute interval for a tomographic epoch were adopted, meaning that SWD
316 observations from seven epochs stacked to one tomographic modelling interval were used −
317 including the two sample data at the two ends of the interval. The reason for the selection of data
318 from May 2015 is that its monthly total rainfall was 513.0 mm, a 68% larger than the normal
319 level of 304.7 mm. The weather in Hong Kong was hot on the first few days of the month. After
320 a cloudy but relatively rain-free day on 8 May, another trough of low pressure brought heavier
321 showers and thunderstorms to Hong Kong on 9-10 May. Two rainstorm episodes on 20 and 23
322 May brought rain to most parts of the Hong Kong. Another rapidly developed rainstorm was on
323 26 May. The weather improved gradually with sunny periods on 28-30 May. However, the
324 weather turned cloudy again with isolated showers and thunderstorms on 31 May. The
325 tomographic scheme for testing is as follows. The first step is to determine the vertical
326 planes/layers for the tomographic field. Non-uniform vertical intervals from 300 to 3800 m (Fig.
327 6(b)) were selected for adaption to the inherent characteristic of water vapor spatial
328 distribution−it exponentially decreases with the increase of height. The use of this structure can
329 also avoid too many unknown parameters overfitting the SWD observations. The next step is to
330 determine the tomographic polygon/boundary on each of the above planes using the methods in
331 section 2.2.1 and based on the GNSS signals in the tomographic interval, then according to the
332 polygon's perimeter, a F_0 value in the force displacement algorithm for determination of the
333 density of nodes on each plane is calculated. All F_0 results in our test are in the range of about
334 1800−10000 m corresponding to the range of height 300–10800 m. The position of the nodes on
335 each plane is determined by Eq. (2).

336   Figure 7 shows the boundary and nodes on three tomographic planes at tomographic
337 epoch UTC 0 on DOY 121, 2015 for an example. Tomographic model results are presented in
338 the next section.
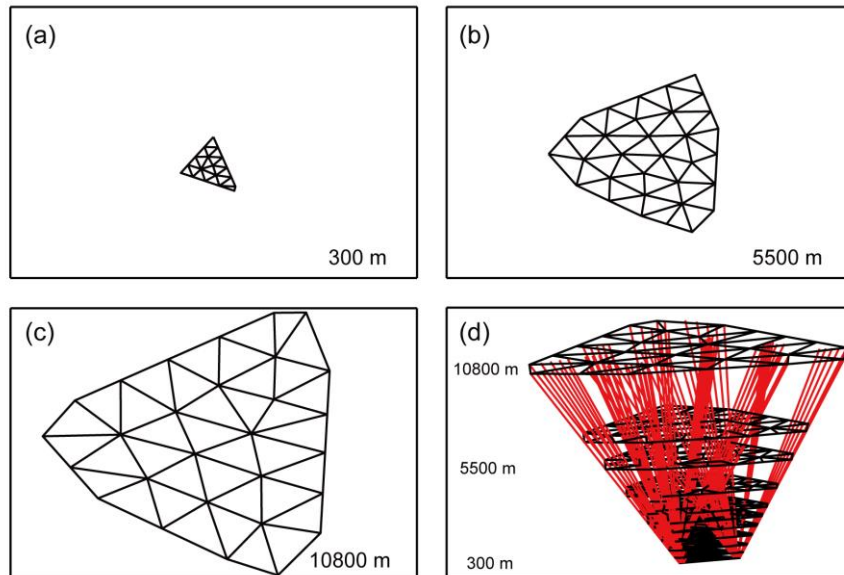
339

340 **Figure 7.** Tomographic boundary and nodes on three planes ((a), (b) and (c)) and the
341 tomographic field and nodes (d) at tomographic epoch UTC 0 on DOY 121, 2015.

342   3.2 Results of profiles

343   Water vapor density values obtained from the tomographic models at tomographic
344   epochs UTC 0 and UTC 12 on each day of the month (DOYs 121−151) were compared against
345   radiosonde (RS) data for evaluation of the model's accuracy. The values of the tomographic
346   results at all RS sampling points were calculated first using the interpolation method mentioned
347   in section 2.2.1, then the root mean square error (RMSE) of the differences between the
348   interpolated values and RS observations at all the sampling points of the RS profile from the
349   ground surface to 10800 m at each epoch was calculated for the accuracy of the profile. All the
350   results at the 62 epochs during the 31-day period are shown in Fig. 8.
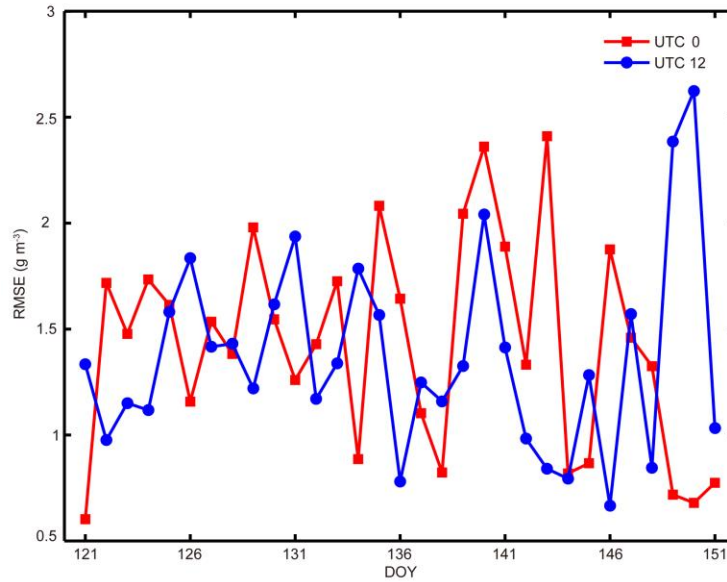
351

352   **Figure 8.** RMSE of model-derived water vapor density values at all RS sampling points of the
353   RS profile below 10800 m at tomographic epochs UTC 0 and UTC 12 on each day of the month
354   (DOYs 121−151).

355

356   The maximum RMSEs, i.e., the worst results, at UTC 0 (red) and UTC 12 (blue) are on
357   DOY 143 and DOY 150 respectively; while the best result (the minimum RMSEs) at the two
358   epochs are on DOYs 121 and 146. In order to find the reason for the large difference between the
359   worst and best results, the tomographic field, the distribution of the signals and the nodes at these
360   four epochs are given in Fig. 9, where Fig. 9(a) and Fig. 9(b) correspond to the best results at
361   UTC 0 and UTC 12 respectively, both of which show uniform distributions of the GNSS signals.
362   However, the distributions of the GNSS signals corresponding to the worst results at UTC 0 (Fig
363   9(c)) and UTC 12 (Fig 9(d)) are different in the sparse signals shown in blue lines, which is one of
364   possible reasons for the poor accuracy of the model results.
365
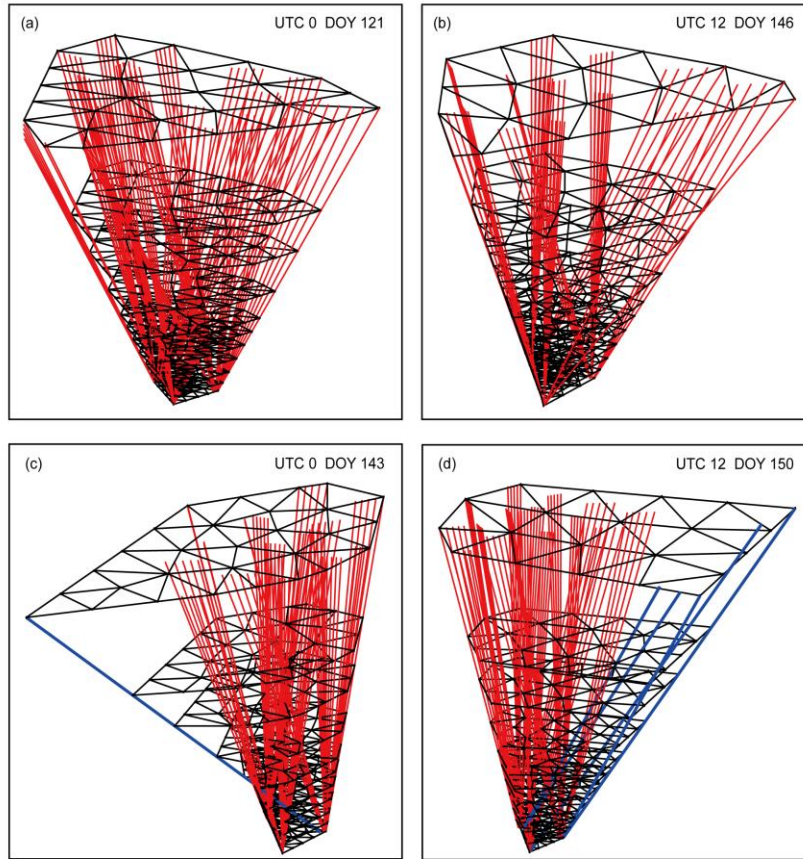
Figure 9. Tomographic field and signal distribution at tomographic epoch UTC 0 on DOY 121 (a), UTC 12 on DOY 146 (b), UTC 0 on DOY 143 (c), and UTC 12 on DOY 150 (d).

The results shown in Fig. 8 are the statistics of the model results for each epoch on each day. In Table 1, the statistics of the model results at both epochs together in the whole month are compared with that of the adaptive node parameterization approach (ANP) (Ding et al., 2018) during the same periods. Unlike the results of new approach are based on three stations of SatRef, 17 stations of SatRef are used to estimate the results of the ANP. The RMSE and IQR values of new approach are similar to that of the ANP, meaning that the new approach for a few GNSS stations, such as three stations, is feasible. But in terms of the Bias, the new approach has a poor performance.

Table 1. Monthly statistics of new approach and ANP

| Statistic	RMSE (g m^{-3})	Bias (g m^{-3})	IQR (g m^{-3})
New approach	1.477	0.239	1.430
ANP	1.216	-0.012	1.678

To indicate the spread of all the errors (the ones used to calculate the above monthly statistics), scatter plots shown in Fig. 10(a) are used to analyze the characteristics of these errors in different intervals. The x and y axes denote the RS observation and the model result (in g m^{-3})

383 respectively; each hollow circle corresponds to a sampling point's result; and the red line
384 represents the "perfect" results, i.e. the model results equal to the RS results. Those hollow
385 circles that are on the red line have an error value of zero, those above the red line have a
386 positive error value, and the rest have a negative error value. The closer a hollow circle to the red
387 line, the smaller its error value.

388 How well all the hollow circles "fit" the red line indicates the overall quality of the model
389 results. It is clear that the hollow circles have a cigar-shaped (fusiform) distribution. The hollow
390 circles in both ending intervals ([0−5] and [20−25] g m^{-3}) more concentrate around the red line
391 than those in the middle part ([5−20] g m^{-3}). The reason for this is 1) most of the sampling points
392 in the [20−25] g m^{-3}interval are located near the ground surface, where water vapor density
393 decreases exponentially with the increase of height and there are about 20 nodes were penetrated
394 by about 106 signals on the bottom of the tomographic region (300m) and 28 nodes were
395 penetrated by the same number of signals on the top of tomographic region (10800m). However,
396 the area of tomographic boundaries on the bottom is about 64 km^2 (i.e., about 1.7 signals per
397 square kilometer) and that on the top is 1550 km^2 (i.e., about 0.07 signals per square kilometer).
398 Therefore, the density of the GNSS signals is very high near the ground surface, which results in
399 relative high accuracy; 2) most of the sampling points in the [5−20] g m^{-3} interval are located in
400 the mid-height of the tomographic field, where the GNSS signals are sparser than the [20−25] g
401 m^{-3} interval, leading to a larger tomographic field, which results in a lower accuracy; and 3)
402 most of the sampling points in the [0−5] interval are located in the top section of the tomographic
403 field, where the water vapor values are smaller than the other two intervals, leading to the
404 smallest errors.
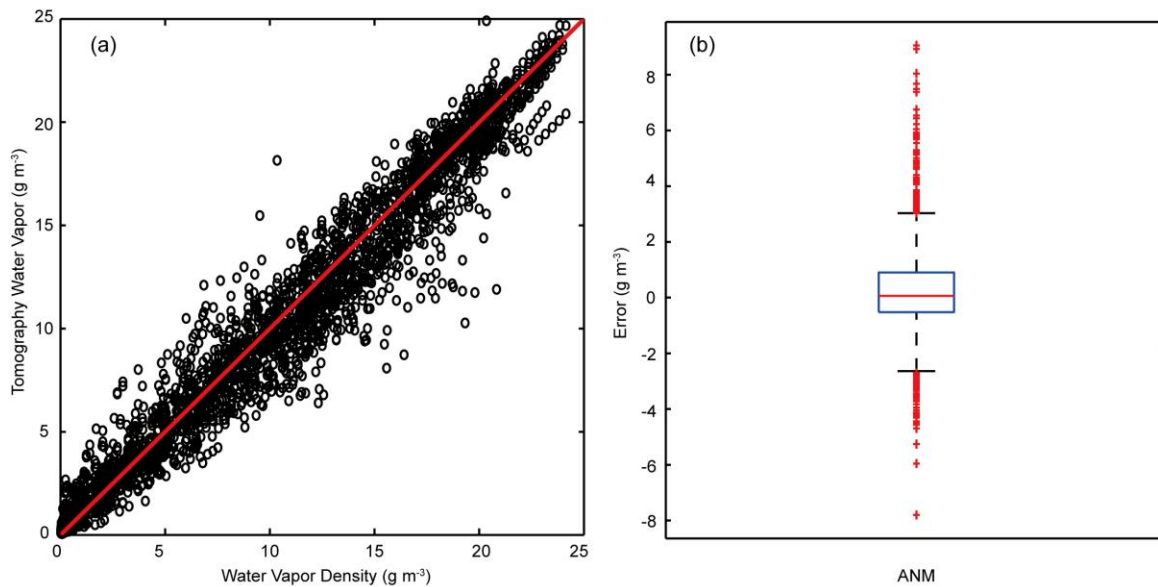
Figure 10. Graphic presentation for the distribution of the tomographic results at the two epochs on every day during the month: (a) scatter plot of water vapor density; and (b) box plot for outlier detection of the tomographic errors.

409 The box plot is mainly for the indication of those large errors at all sampling points. Q1
410 and Q3, which are the first and third quartiles respectively, determine the IQR value in Table 1;
411 Q2, the second quartile, roughly reflects the bias of all the errors; the whiskers, i.e. the two black

412　bars, located at Q1−1.5(IQR) and Q3+1.5(IQR), are for the determination of the lower and upper
413　bounds of the criteria for outlier detection, e.g. the red cross marks are regarded outliers. Table 2
414　lists all the above characteristic values of all errors (the total number of errors is 2790).

415

416　**Table 2.** Characteristic values of the box plots in Fig. 10(b).

417

Statistic	Q1 (g m^{-3})	Q2 (g m^{-3})	Q3 (g m^{-3})	Upper bound (g m^{-3})	Lower bound (g m^{-3})	Number of outliers
	−0.527	0.062	0.903	3.048	−2.672	159

418

419　3.3 Results of different layers

420　　　In the last section, the RMSE of model-derived water vapor density values at all sampling
421　points for each profile (Fig. 8) and the errors at all the sampling points and two epochs on each
422　day during the month (Fig. 9) are analyzed for the assessment of the overall performance of the
423　models. In this section, the monthly RMSE at all the sampling points but in 11 different
424　tomographic layers and the monthly mean of the relative errors in these layers are investigated,
425　see Fig. 11.

426　　　In those layers below 1500 m, the two lines in both subfigures show the same tendency of
427　variation with height −the error value increases with the increase of height. This is because the
428　higher the layer, the more the spread of the GNSS signals, the worse the accuracy of the result.
429　However, in the layers above 1500 m, the two lines show opposite tendencies of variation with
430　height because the higher, the smaller the water vapor density. The smaller water vapor density
431　values in these high layers lead to the small RMSE and large relative errors.
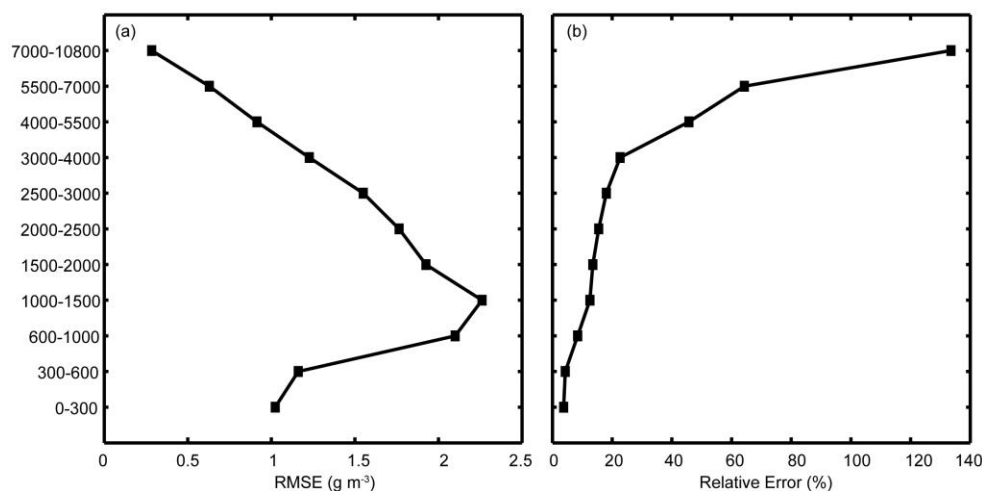
432

433　**Figure 11.** (a) Monthly RMSE of (absolute) tomographic errors and (b) mean of relative
434　tomographic errors in different layers.

435

4 Conclusion and outlook

In this study a new node parameterization approach for determination of a tomographic field based on the distribution of GNSS signals at the tomographic epoch and also for discretization of the tomographic field is proposed. The number and the position of the nodes on each tomographic plane are determined based on the perimeter of the tomographic boundary on the plane and meshing techniques respectively. Since the tomographic model is tailor-made for the tomographic field at the epoch, the new approach is applicable to not only GNSS networks with several stations, but also GNSS networks with few stations, e.g., three stations, which cannot be solved by conventional approaches. The new approach was tested using GNSS data from three stations in the Hong Kong Satellite Positioning Reference Station Network during the period of May, 2015 and its model results were validated by comparing them against radiosonde data at UTC 0 and UTC 12 from HKKP. Results suggest that the new approach is feasible for a three-station GNSS network. In addition, monthly statistics of the tomographic results on each tomographic layer indicated that the size of the tomographic boundary and the magnitude of water vapor are two critical factors affecting the accuracy of the tomographic result of the layer.

Our future work will be focusing on using unevenly distributed nodes that fit the density of the GNSS signals.

Data availability

GNSS data in the RINEX format used for this study can be downloaded from website (http://www.geodetic.gov.hk/smo/gsi/programs/en/GSS/satref/satref.htm). Radiosonde data of King's Park Meteorological Station can be downloaded from website (http://weather.uwyo.edu/upperair/sounding.html).

Author Contribution

- Nan Ding contributes to conceptualization, data curation, formal analysis, investigation, methodology, resources, software, validation, visualization, writing-original draft and writing-review & editing.

- Shubi Zhang contributes to conceptualization, formal analysis, funding acquisition, methodology, project administration, resources, supervision, writing-original draft and writing-review & editing.

- Suqin Wu contributes to formal analysis, supervision, writing-original draft and writing-review & editing.

- Xiaoming Wang contributes to conceptualization, formal analysis, investigation, methodology, resources, validation, writing-original draft and writing-review & editing.

- Xin Liu data curation, investigation, methodology, resources, visualization, writing-original draft and writing-review & editing.

- Allison Kealy contributes to formal analysis, methodology, resources, supervision, writing-original draft.

16

475 ● Kefei Zhang contributes to conceptualization, formal analysis, funding acquisition,
476 investigation, project administration, resources, supervision, writing-original draft and
477 writing-review & editing.

478

Competing interests

480 The authors do not have any possible conflicts of interest.

Acknowledgements

489

References

491 Bastin, S., Champollion, D., Bock, O., Drobinski, P., and Masson, F.: On the use of GPS
492 tomography to investigate water vapor variability during a Mistral/sea breeze event in
493 southeastern France, GEOPHYS. RES. LETT., 32,
494 https://doi.org/10.1029/2004GL021907, 2005.

495 Bender, M., Dick, G., Wickert, J., Ramatschi, M., Ge, M., Gendt, G., Rothacher, M., Raabe, A.,
496 and Tetzlaff, G.: Estimates of the information provided by GPS slant data observed in
497 Germany regarding tomographic applications, J. GEOPHYS. RES., 114,
498 https://doi.org/10.1029/2008JD011008 , 2009.

499 Bender, M., Stosius, R., Zus, F., Dick, G., Wickert, J., and Raabe, A.: GNSS water vapour
500 tomography – Expected improvements by combining GPS, GLONASS and Galileo
501 observations, ADV. SPACE. RES., 47, 886-897,
502 https://doi.org/10.1016/j.asr.2010.09.011, 2011.

503 Bevis, M., Businger, S., Chiswell, S., Herring, T. A., Anthes, R. A., Rocken, C., and Ware, R. H.:
504 GPS meteorology: Mapping zenith wet delays onto precipitable water, J. APPL.
505 METEOROL., 33, 379-386, https://doi.org/10.1175/1520-
506 0450(1994)033<0379:GMMZWD>2.0.CO;2, 1994.

507 Champollion, C., Masson, F., Bouin, M. N., Walpersdorf, A., Doerflinger, E., Bock, O., and Van
508 Baelen, J.: GPS water vapour tomography: preliminary results from the ESCOMPTE
509 field experiment, ATMOS. RES., 74, 253-274,
510 https://doi.org/10.1016/j.atmosres.2004.04.003, 2005.

511 Chen, B., and Liu, Z.: Voxel-optimized regional water vapor tomography and comparison with
512 radiosonde and numerical weather model, J. GEODESY., 88, 691-703,
513 https://doi.org/10.1007/s00190-014-0715-y, 2014.

17

Chen, B., Liu, Z., Wong, W., and Woo, W.: Detecting Water Vapor Variability during Heavy
    Precipitation Events in Hong Kong Using the GPS Tomographic Technique, J. ATMOS.
    OCEAN. TECH., 34, 1001-1019, https://doi.org/10.1175/JTECH-D-16-0115.1, 2017.

Delanue, B.: Sur la sphère vide. A la mémoire de Georges Voronoï, Bulletin de l'Académie des
    Sciences de l'URSS. Classe des sciences mathématiques et na, 6, 793–800, available at:
    http://www.mathnet.ru/links/e8a3b79d32e0796cb49d8f84ecc72b6f/im4937.pdf, 1934

Ding, N., Zhang, S. B., Wu, S. Q., Wang, X. M., and Zhang, K. F.: Adaptive Node
    Parameterization for Dynamic Determination of Boundaries and Nodes of GNSS
    Tomographic Models, J. GEOPHYS. RES-ATMOS., 123.4,
    https://doi.org/10.1002/2017JD027748, 2018.

Ding, N., Zhang, S., and Zhang, Q.: New parameterized model for GPS water vapor tomography,
    ANGEO., 35, 311-323, https://doi.org/10.5194/angeo-35-311-2017, 2017.

Edelsbrunner, H., Li, X. Y., Miller, G., Stathopoulos, A., Talmor, D., Teng, S. H., Üng R, A.,
    and Walkington, N.: Smoothing and cleaning up slivers. ACM Symposium on Theory of
    Computing, DOI: 10.1145/335305.335338, 2000.

Flores, A., Ruffini, G., and Rius, A.: 4D tropospheric tomography using GPS slant wet delays,
    ANN. GEOPHYS-ATM. HYDR., 18, 223-234, https://doi.org/10.1007/s00585-000-
    0223-7, 2000.

Gradinarsky, L. P.: Sensing atmospheric water vapor using radio waves, Chalmers University of
    Technology, 90-106, available at: https://elibrary.ru/item.asp?id=5917695, 2002.

Gradinarsky, L. P., and Jarlemark, P.: Ground-based GPS tomography of water vapor: Analysis
    of simulated and real data, J. METEOROL. SOC. JPN., 82, 551-560,
    https://doi.org/10.2151/jmsj.2004.551, 2004.

Graham, R. L.: An efficient algorithm for determining the convex hull of a finite planar set,
    INFORM. PROCESS. LETT., 4(1), 132–133, https://doi.org/10.1016/0020-
    0190(72)90045-2, 1972.

Hoyle, V. A.: Data assimilation for 4-D wet refractivity modelling in a regional GPS network,
    University of Calgary, Department of Geomatics Engineering, 139–150,
    http://dx.doi.org/10.5072/PRISM/17377, 2005.

Kaczmarz, S.: Angenäherte auflösung von systemen linearer gleichungen, Bulletin International
    de l'Academie Polonaise des Sciences et des Lettres, 35, 355-357, available at:
    http://jasonstockmann.com/Jason_Stockmann/Welcome_files/kaczmarz_english_translati
    on_1937.pdf, 1937.

Perler, D., Geiger, A., and Hurter, F.: 4D GPS water vapor tomography: new parameterized
    approaches, J. GEODESY., 85, 539-550, DOI: 10.1007/s00190-011-0454-2, 2011.

Persson, P.: Mesh generation for implicit geometries, Massachusetts Institute of Technology,
    available at: https://dspace.mit.edu/bitstream/handle/1721.1/27866/60503856-MIT.pdf,
    2005.

Rohm, W., and Bosy, J.: Local tomography troposphere model over mountains area,
    https://doi.org/10.1016/j.atmosres.2009.03.013, ATMOS. RES., 93, 777-783, 2009.

554 Rohm, W., Zhang, K., and Bosy, J.: Limited constraint, robust Kalman filtering for GNSS
555   troposphere tomography, ATMOS. MEAS. TECH., 7, 1475-1486,
556   https://doi.org/10.5194/amt-7-1475-2014, 2014.

557 Saastamoinen, J.: Atmospheric correction for the troposphere and stratosphere in radio ranging
558   satellites, The use of artificial satellites for geodesy, 247-251,
559   https://doi.org/10.1029/GM015p0247, 1972.

560 Seko, H., Shimada, S., Nakamura, H., and Kato, T.: Three-dimensional distribution of water
561   vapor estimated from tropospheric delay of GPS data in a mesoscale precipitation system
562   of the Baiu front, EARTH PLANETS. SPACE., 52, 927-933,
563   https://doi.org/10.1186/BF03352307, 2000.

564 Troller, M., Geiger, A., Brockmann, E., Bettems, J. M., Burki, B., and Kahle, H. G.:
565   Tomographic determination of the spatial distribution of water vapor using GPS
566   observations. In: Burrows, J. P., Eichmann, K. U., and LLewellyn, E. J., ASR.,
567   https://doi.org/10.1016/j.asr.2005.07.002, 2006.

568 Wang, X., Zhang, K., Wu, S., Fan, S., and Cheng, Y.: Water vapor‐weighted mean temperature
569   and its impact on the determination of precipitable water vapor and its linear trend, J.
570   GEOPHYS. RES-ATMOS., 121, 833-851, https://doi.org/10.1002/2015JD024181, 2016.

571 Wang, X., Zhang, K., Wu, S., He, C., Cheng, Y., and Li, X.: Determination of zenith hydrostatic
572   delays and the development of new global long-term GNSS-derived precipitable water
573   vapor, ATMOS. MEAS. TECH., 1-17, https://doi.org/10.5194/amt-10-2807-2017, 2017.

574 Xia, P., Cai, C., and Liu, Z.: GNSS troposphere tomography based on two-step reconstructions
575   using GPS observations and COSMIC profiles. ANGEO., Copernicus GmbH,
576   https://doi.org/10.5194/angeo-31-1805-2013, 2013.

577 Yao, Y. B., Zhao, Q. Z., and Zhang, B.: A method to improve the utilization of GNSS
578   observation for water vapor tomography, ANN. GEOPHYS-GERMANY., 34, 143-152,
579   https://doi.org/10.5194/angeo-34-143-2016, 2016.

580 Ye, S., Xia, P., and Cai, C.: Optimization of GPS water vapor tomography technique with
581   radiosonde and COSMIC historical data, 34, ANGEO., 789-799,
582   https://doi.org/10.5194/angeo-34-789-2016, 2016.

583 Zhang, K., Manning, T., Wu, S., Rohm, W., Silcock, D., and Choy, S.: Capturing the Signature
584   of Severe Weather Events in Australia Using GPS Measurements, IEEE. J-STARS., 8,
585   1839-1847, DOI: 10.1109/JSTARS.2015.2406313, 2015.